Soft Matter

ROYAL SOCIETY OF CHEMISTRY

PAPER

View Article Online
View Journal | View Issue

Cite this: *Soft Matter*, 2026, 22, 3081

Symmetry-breaking motility of an active hinge in a crowded channel

Leonardo Garibaldi Rigon and Yongjoo Baek*

Received 19th June 2025,
Accepted 6th April 2026

DOI: 10.1039/d5sm00622h

rsc.li/soft-matter-journal

A recent experiment [K. Son, Y. Choe, E. Kwon, L. G. Rigon, Y. Baek and H.-Y. Kim, *Soft Matter*, 2024, **20**, 2777–2788] showed that self-propelled particles confined within a circular boundary filled with granular medium spontaneously form a motile cluster that stays on the boundary. This cluster exhibits persistent (counter)clockwise motion driven by symmetry breaking, which arises from a positive feedback between the asymmetry of the cluster and those of the surrounding granular medium. To investigate this symmetry-breaking mechanism in broader contexts, we propose and analyze the dynamics of an active hinge moving through a crowded two-dimensional channel. Through extensive numerical simulations, we find that the lifetime of the hinge's motile state varies nonmonotonically with the packing fraction of the granular medium. Furthermore, we observe an abrupt transition in the configuration of passive particles that sustain hinge motility as the hinge's maximum angle relative to the channel wall increases. These findings point to the possibility of designing superstructures composed of passive granular media doped with a small number of active elements, whose dynamic modes can be switched by tuning the properties of their components.

1 Introduction

Active matter encompasses a broad class of nonequilibrium systems in which the constituent particles, called active particles, consume energy to generate motion.[1–8] When subjected to spatially asymmetric environments, like a ratchet potential, such active particles produce nonequilibrium currents in the steady state, a phenomenon known as current rectification[9–12] that has found applications in the design of targeted delivery systems[13] and self-starting micromotors.[14–16] However, even when the environments are perfectly symmetric, nonequilibrium currents can still emerge through symmetry breaking. This can occur by active particles self-organizing themselves to form asymmetric structures,[17,18] by a rigid passive object experiencing a negative drag exerted by the surrounding active particles,[19–22] or by active particles deforming a soft passive object (like polymer chains) to form an asymmetric structure.[23–26]

Meanwhile, vibrated granular particles form an important subclass of active matter. In addition to possessing both liquid-like and solid-like properties like other granular systems,[27] they are known to exhibit collective motion,[28–33] clustering,[33–36] crystallization,[37] demixing,[38] and nontrivial dynamics of topological defects.[39] If such systems consist of a small number of active dopants ("active" in the sense that they propel themselves in the direction of their polarity) mixed with a majority of passive granular particles ("passive" in the sense that they are isotropic and lack any persistent propulsion direction, despite being possibly athermal), the interplay between the active and passive granular particles have been shown to promote crystallization,[40,41] facilitate the removal of grain boundaries in polycrystals,[42] and induce coherent particle transport called "flocking".[43,44]

In particular, to observe flocking using a vibrated granular medium in a two-dimensional confinement, it is well known that the confinement boundary has to be shaped like petals[30,31] to prevent the accumulation of a large, static cluster of active particles.[29,46–48] However, Son *et al.*[45] found that a sufficiently small number of elliptical active particles, which propel themselves along the major axis, can form a coherent, motile boundary cluster that moves persistently in one direction (clockwise or counterclockwise) even in a perfectly circular confinement lacking petals. This phenomenon can be understood as follows: as illustrated in the upper panel of Fig. 1a, active particles (pink ellipses) pushing against the confinement boundary (with self-propulsion directions marked by thick white arrows) may accidentally form an asymmetric cluster with a passive disk stuck at one end of the cluster. Due to the asymmetric shape of the cluster, the net propulsion force (thin pink arrow) pushes the cluster against the passive disk, keeping it attached to the front. In turn, the passive disk prevents the adjacent active particle from leaning against the boundary, thereby keeping the asymmetric shape of the cluster. This feedback loop breaks the symmetry and stabilizes the motile

---

Department of Physics and Astronomy & Center for Theoretical Physics, Seoul National University, Seoul 08826, Korea. E-mail: y.baek@snu.ac.kr

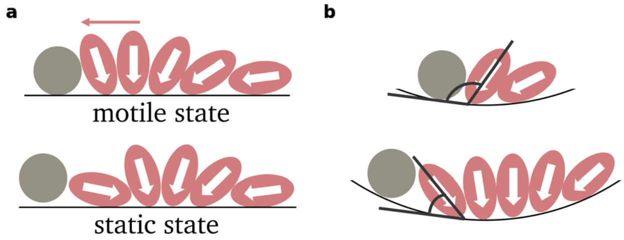

Fig. 1 Schematics of the self-propelled particle cluster reported in Son *et al.*[45] (a) The moving state persists as long as a disk stays stuck in front of the cluster, maintaining its asymmetric shape. Once the disk is removed, the cluster loses the asymmetry and is stuck in a static state. (b) The angle formed by the wall and the foremost particle of the cluster is an important factor determining the lifetime of the motile state.

state of the active particle cluster. The cluster can become static only when the passive disk accidentally moves away from the cluster, allowing the neighboring active particle to lean against the boundary and make the cluster symmetric, see the lower panel of Fig. 1a. How quickly this happens depends on the typical angle between the active particle adjacent to the passive disk and the confinement boundary—when the angle is smaller, the cluster becomes more symmetric and less motile, making it easier for the passive disk to escape. As illustrated in Fig. 1b, this angle is determined by the interplay between the active particle cluster size and the boundary curvature, decreasing as more active particles join the cluster. Indeed, Son *et al.*[45] found that the persistence of the motile state decreases dramatically when the number of active particles increases beyond a certain threshold.

When current rectification arises from symmetry-breaking mechanisms, persistence of the resulting motile structures may exhibit nonmonotonic dependence on the parameters describing constituent particles since symmetry breaking may occur only when such parameters fall within limited ranges. This can reveal effective methods for designing superstructures with tunable dynamical properties. In this study, by introducing a simplified model called the active hinge model, we further investigate how the persistence of the symmetry-broken structure is affected by the physical properties of the active and passive granular particles. We find that the cluster's directional persistence varies nonmonotonically with the packing fraction of the granular medium. Moreover, we observe that the passive particle configuration responsible for the persistence of the motile state exhibits an abrupt change as the maximum angle between the hinge and the channel wall increases, which is a close analog of how the boundary cluster in the experiment of Son *et al.*[45] suddenly loses motility as the number of active particles increases.

The remainder of this paper is organized as follows. In Section 2, we introduce the model and simulation details. Section 3 focuses on the emergence of the motile state sustained by a symmetry-breaking mechanism. In Section 4, we present a detailed analysis of the persistence of this motile state, focusing on its dependence on the packing fraction of the medium (Section 4.1) and the maximum hinge angle (Section 4.2) while also discussing the effects of the active force magnitude, the rod length, and the hinge mobility. Finally, in Section 5, we discuss the implications of our findings and outline possible directions for future research.

2 Active hinge model

As a simplified description of the experimental system discussed in Son *et al.*,[45] we propose the active hinge model, which focuses on the dynamics of the self-propelled particle (SPP) cluster after it is formed at the boundary of the system. The model features two identical self-propelled, overdamped rods connected by a sliding hinge and immersed in a bath of overdamped passive Brownian disks confined in a two-dimensional channel with periodic boundaries in the x direction and rigid, confining walls in the y direction. Imitating the behavior of the active elliptical particles at both ends of the boundary cluster observed in Son *et al.*,[45] each rod exerts a constant active force (self-propulsion) of magnitude F_{act} along its body toward the hinge, its orientation fluctuating as it collides with the passive disks. The hinge stays attached to a channel wall, moving only along the x direction. The whole setup is illustrated in Fig. 2. Throughout this study, taking the diameter of the passive disk, σ, as the unit length, we fix the dimensions of the system at $L_x = L_y = 10\sigma$.

In the SPP clusters observed in the experiment,[45] due to the circular curvature of the wall and the elliptical shape of the SPPs, the effective maximum angle formed by the wall and the body axis of an SPP at the cluster boundary decreased as the cluster size increased (see Fig. 1). To reproduce this effect, we introduce an upper bound, $\theta_{\max}$, on the angle between each rod and the wall (so that $\theta_{\mathrm{L,R}} \le \theta_{\max}$), as indicated by dashed lines in Fig. 2b.

In accordance with these descriptions, the horizontal location x_{act}, the angle θ formed by each rod and the wall, and the position $\mathbf{x}_{\mathrm{pas}}$ of each passive disk obey the overdamped Langevin equations

$$\boldsymbol{\Gamma}\begin{pmatrix}\dot{x}_{\mathrm{act}}\\ \dot{\theta}_{\mathrm{L}}\\ \dot{\theta}_{\mathrm{R}}\end{pmatrix} = \begin{pmatrix}F_{\mathrm{tot},x}\\ \tau_{\mathrm{L}}\\ \tau_{\mathrm{R}}\end{pmatrix}, \tag{1}$$

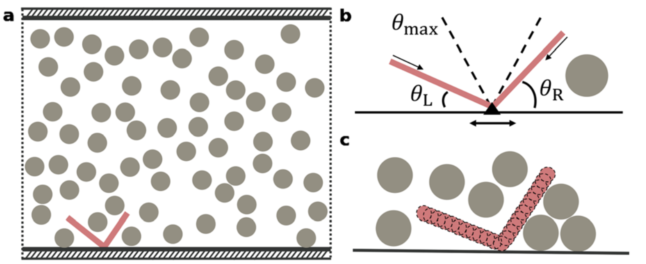

Fig. 2 A schematic illustration of the active hinge model. (a) The active hinge, highlighted in red, is immersed in a bath of passive Brownian particles confined within a two-dimensional channel. (b) A detailed view of the active hinge showing the angle parameters. (c) An example of an asymmetric hinge–disk cluster that would propelled to the right.

$$\mu_{\rm pas}{}^{-1}\dot{\mathbf{x}}_{\rm pas} = \mathbf{F}^{\rm pas}_{\rm int} + \sqrt{2D}\boldsymbol{\xi}. \tag{2}$$

Here $\boldsymbol{\Gamma}$ is the drag matrix, $F_{{\rm tot},x}$ the x-component of the net force on the hinge that includes the self-propulsion forces of the rods and interactions with the passive disks, $\tau_{\rm L}$ and $\tau_{\rm R}$ the torques applied on the left and right rods, respectively, by the passive disks, $\mathbf{F}^{\rm pas}_{\rm int}$ the total force exerted upon a passive disk by the wall, the self-propelled rods, and the other passive disks, D the diffusion coefficient, and $\boldsymbol{\xi}$ the random force whose components are independent Gaussian white noises of unit amplitude. We assume that each rod can be regarded as a rigid chain of M identical disks (excluding the central disk connecting the rods), with the x-components of the self-propulsion forces given by $F_{\rm act}\cos\theta_{\rm L}$ for the left rod and $-F_{\rm act}\cos\theta_{\rm R}$ for the right rod. The chain beads have a different mobility, μ, than the passive disks. The drag matrix $\boldsymbol{\Gamma}$, as derived in Appendix A, has nonvanishing off-diagonal terms which couple translation to the torques and rotation to the force. In the simulations, we calculate the values of $F_{{\rm tot},x}$, $\tau_{\rm L/R}$, and $\mathbf{F}^{\rm pas}_{\rm int}$ based on the following assumptions:

(1) Each rod is composed of overlapping disks of radius 0.1σ with the centers of adjacent disks spaced at 0.1σ.

(2) A pair of disks separated by a center-to-center distance r_{ij} interact *via* the Weeks–Chandler–Andersen (WCA) potential

$$U(r_{ij}) = \begin{cases} 4\varepsilon\left[\left(\dfrac{\sigma_{ij}}{r_{ij}}\right)^{12} - \left(\dfrac{\sigma_{ij}}{r_{ij}}\right)^{6}\right] & \text{if } r_{ij} \le 2^{1/6}\sigma_{ij}, \\ 0 & \text{otherwise.} \end{cases} \tag{3}$$

Here, σ_{ij} represents the sum of the radii of two interacting objects. Also note that, in the case of disk–wall interactions, r_{ij} represents the distance between the center of the disk and the wall. In our study, we use $\varepsilon = 5k_{\rm B}T$ and $\sigma_{ij} = \sigma$ for interactions between passive disks as well as disk–wall interactions, while $\varepsilon = 0.5k_{\rm B}T$ and $\sigma_{ij} = 0.6\sigma$ are used for interactions between passive disks and the disks forming the self-propelled rods.

Then, by multiplying $\boldsymbol{\Gamma}^{-1}$ to the calculated forces and torques, we obtain the instantaneous displacement $(\dot{x}_{\rm act},\dot{\theta}_{\rm L},\dot{\theta}_{\rm R})\Delta t$, where Δt is the discretized time step.

We ensure that both $\theta_{\rm L}$ and $\theta_{\rm R}$ stay in the range $[0,\theta_{\rm max}]$ by explicitly including the needed constraint force in the equations of motion whenever an update is about to violate the angular constraints. See the description at the end of Appendix A for more detail. Once either $\theta_{\rm L}$ or $\theta_{\rm R}$ reaches zero, the corresponding rod stays attached to the wall since no passive disks can split them apart. Thus, the active hinge reaches an absorbing state once both angles become zero.

For all the numerical results, we take σ and $k_{\rm B}T$ as the units of length and energy, respectively. According to this choice, the Péclet number ${\rm Pe} \equiv F_{\rm act}\sigma/(k_{\rm B}T)$ can be regarded as the dimensionless self-propulsion force. We also choose $\tau = \sigma^2/D = \sigma^2/(\mu_{\rm pas}k_{\rm B}T)$ as the unit of time. Then we set the discretized time step to be $\Delta t = 10^{-2}\tau$, run every simulation from $t = 0$ to $t = 5 \times 10^5\tau$, and take the ensemble average over $N_{\rm sim} = 200$ samples. If the values of the observables are presented without any units, they are based on the unit system that fixes $\sigma = k_{\rm B}T = \tau = 1$ (with the last equality ensured by setting $\mu_{\rm pas} = 1$).

3 Symmetry-breaking motility of the hinge

We first demonstrate that the active hinge exhibits a motile state maintained by a symmetry-breaking mechanism. Toward this aim, we simulate the system starting from the symmetric configuration with $\theta_{\rm L,R} = \theta_{\rm max}$ (with the passive disks having reached a steady state under this constraint) and then measure the mean first-passage times (MFPTs) for each angle to reach zero. Let us call the rod whose angle with the wall reaches zero first the 'first rod', while the other is called the 'second rod'. The MFPT of the first rod refers to the average period of time between the beginning of the observation and the absorption of the first rod. The MFPT of the second rod refers to the average period of time between the absorption of the first rod and that of the second rod. See Fig. 3 for a schematic of the idea and Appendix B for how the MFPT is estimated.

In Fig. 4, we observe that under various conditions the MFPT of the first rod is much shorter than that of the second rod. As shown in Fig. 4a, for the intermediate regime of packing fraction ϕ of the passive disks the MFPT of the first rod monotonically increases with ϕ, reflecting that the increased collisions with the background medium slows down the absorption of the first rod. This is in contrast to the MFPT of the second rod, which exhibits nonmonotonic dependence on ϕ as shown in Fig. 4b. This suggests multiple competing mechanisms that promote or inhibit the motile state of the hinge, which will be discussed in more detail in the next section.

The mean squared displacement (MSD) of the hinge also corroborates the existence of the motile state. As Fig. 5a shows, the hinge undergoes normal diffusion until the first rod is absorbed. Then, as shown in Fig. 5b, the motion stays ballistic

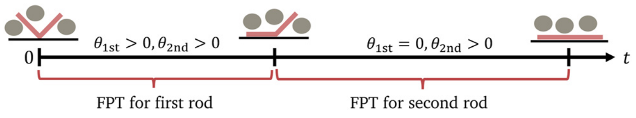

Fig. 3 Design of the simulation. Starting from the symmetric hinge configuration, two first-passage times (FPTs) can be defined depending on which rod is absorbed.

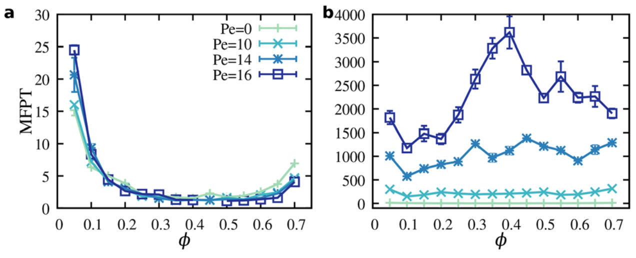

Fig. 4 Mean first-passage time (MFPT) of the (a) first and the (b) second rods as a function of the packing fraction ϕ for different self-propulsion strengths Pe. We use $\theta_{\rm max} = 60°$, $l = 2$, and $\mu = 40$. The error bars indicate the standard deviations, and the lines are to guide the eye.

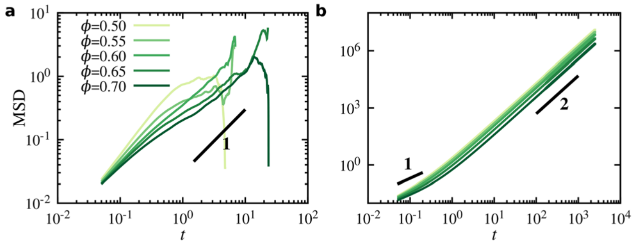

Fig. 5 Mean square displacement (MSD) of the hinge for different packing fractions ϕ (a) up to the absorption of the first rod and (b) up to the absorption of the second rod. The thick black segments with numbers are for comparisons with normal diffusion (MSD ∼ t) and ballistic motion (MSD ∼ t^2). We use Pe = 16, $\theta_{\max}$ = 60°, l = 2, and μ = 40.

for a much longer period of time, which corresponds to the persistent motile state. These results indicate that, once the first rod is absorbed, the hinge enters a motile state maintained by the broken symmetry, as was the case for the experimental system discussed in Son *et al.*[45]

4 Persistence of the motile state

To further investigate the multiple competing mechanisms that contribute to the persistence of the motile state, from now on we focus on the case where the first rod is absorbed from the beginning while the initial angle of the second rod is given by $\theta_{\max}$. Under this condition, we examine the MFPT of the second rod as an indicator of the lifetime of the motile state for various values of the packing fraction ϕ and the maximum angle $\theta_{\max}$.

4.1 Effects of the packing fraction

The packing fraction ϕ, defined as the total area fraction covered by the passive disks, controls how frequently the active hinge interacts with the granular medium. In Fig. 6, we show the ϕ dependence of the lifetime of the motile state as we vary the dimensionless active force Pe, the rod length l, the maximum angle $\theta_{\max}$, and the mobility μ of each disk forming the active rod. When Pe, l, $\theta_{\max}$, or μ is very small, the MFPT achieves the lowest value in the intermediate range of ϕ, while tending to increase as ϕ approaches 0 or the jamming transition (near ϕ = 0.7). On the other hand, if all of these four quantities are sufficiently large, we observe a pronounced peak of the MFPT in the intermediate range of ϕ. These results indicate that large Pe, l, $\theta_{\max}$, and μ activate a mechanism that stabilizes the motile state in the intermediate range of ϕ.

To further investigate the origins of these behaviors, we represent the state of the active hinge using the number of passive disks whose center falls in the circular sector of radius l (*i.e.*, the length of each rod) between the surviving rod and the channel wall. Denoting this number by N, we estimate the average time spent in each state T_N from the simulation data using the method described in Appendix B. This allows us to examine the detailed structure of the MFPT, which is equal to the sum of T_N over all possible values of N.

As shown in Fig. 7a and b, when $\theta_{\max}$ = 45°, only T_0 and T_1 account for most of the MFPT. This is because $\theta_{\max}$ is not large enough to allow more than a single passive disk between the rod and the wall. The monotonic decrease of T_0 with increasing ϕ can be attributed to the increasing rate of collision with the passive disks that accelerate the rotational dynamics of the rod. Meanwhile, the monotonic increase of T_1 with increasing ϕ is due to the crowding of the channel slowing down the escape of the passive disk between the rod and the wall. These behaviors are qualitatively the same regardless of whether the hinge is passive [Pe = 0, as in Fig. 7a] or active [Pe = 16, as in Fig. 7b]. Even if we increase $\theta_{\max}$ to 60°, we still observe essentially similar behaviors as long as Pe is weak.

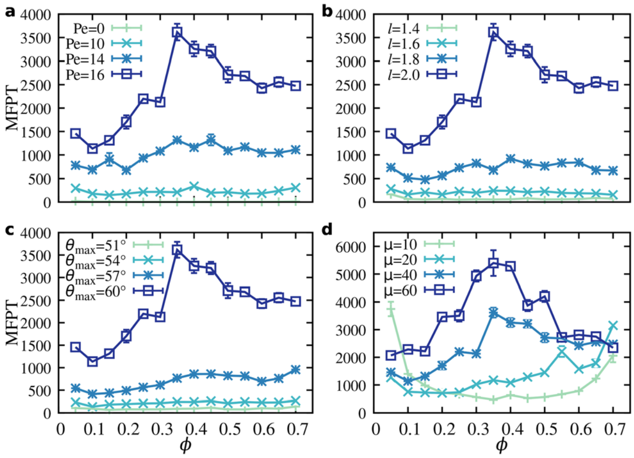

Fig. 6 Lifetime of the motile state indicated by the mean-first passage time (MFPT) as a function of the packing fraction for different values of the active force magnitude Pe, the rod length l, the maximum angle $\theta_{\max}$, and the mobility μ of each disk forming the active rod. For each plot, the fixed parameters are as follows: (a) l = 2, $\theta_{\max}$ = 60°, μ = 40; (b) Pe = 16, $\theta_{\max}$ = 60°, μ = 40; (c) Pe = 16, l = 2, μ = 40; (d) Pe = 16, l = 2, $\theta_{\max}$ = 60°. The error bars indicate the standard deviations, and the lines are to guide the eye.

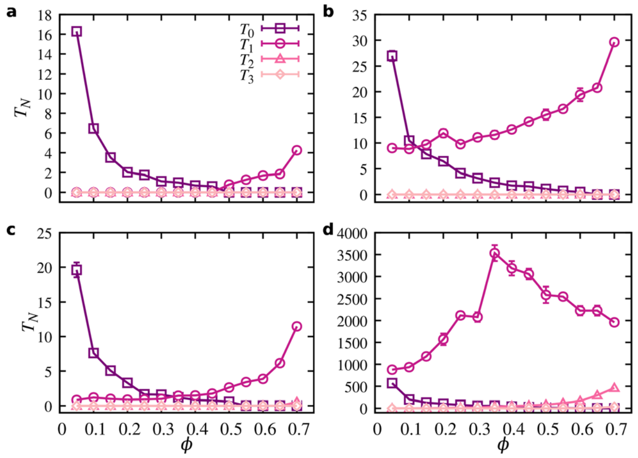

Fig. 7 Average time spent in each coarse-grained state N until absorption as the packing fraction is varied. We fix l = 2, μ = 40 and show the results for (a) $\theta_{\max}$ = 45° and Pe = 0, (b) $\theta_{\max}$ = 45° and Pe = 16, (c) $\theta_{\max}$ = 60° and Pe = 0, and (d) $\theta_{\max}$ = 60° and Pe = 16. The error bars indicate the standard deviations, and the lines are to guide the eye.

Notable changes occur only when both $\theta_{\max}$ and Pe are large enough, as shown in Fig. 7d for $\theta_{\max} = 60^\circ$ and Pe = 16. In this case, the configuration with $N = 1$ achieves a prolonged lifetime even for small values of ϕ, with T_1 dominating the MFPT for an intermediate range of ϕ. This can be attributed to the positive feedback between cluster asymmetry and motility analogous to the mechanism that induced the symmetry-breaking motility in the experiment of Son *et al.*,[45] which was illustrated in Fig. 1. This mechanism requires that the passive disk stuck between the motile active hinge and the wall tends to stay trapped there. This tendency becomes strong when the following are all true.

- The hinge propulsion (governed by Pe) is strong enough, so that the hinge–disk cluster achieves a large horizontal speed. Then, in the frame of reference comoving with the cluster, the disk experiences a large horizontal force towards the hinge (note that, due to the background medium exerting friction, the Gallilean invariance does not hold in this system), which makes it more likely to stay trapped between the hinge and the wall.
- The active rod is long enough (*i.e.*, l is large enough), so that the passive disk finds it difficult to escape the depth of the trap.
- The maximum allowed angle between the active rod and the wall is large enough (*i.e.*, $\theta_{\max}$ is large enough), so that the strong hinge asymmetry helps the hinge–disk cluster achieve a sufficiently large horizontal velocity, strengthening the trapping force.
- The mobility of the hinge in large enough (*i.e.*, μ is large enough), so that the hinge–disk cluster achieve a sufficiently large horizontal velocity, strengthening the trapping force.

These considerations explain why the motile cluster is stabilized for an intermediate range of ϕ when Pe, l, $\theta_{\max}$, and μ are all large enough, as shown in Fig. 6.

One may still ask why the MFPT of the hinge–disk cluster exhibits a peak at an intermediate value of ϕ, starting to decrease again when ϕ goes over a certain threshold. This can be explained by the following reasoning. As the system becomes more crowded, stronger pressure is applied on the rod by the disks above the hinge, which tends to decrease the rod–wall angle, weaken the asymmetry of the motile cluster, and slow it down. This weakens the effective force trapping the passive disk between the rod and the wall, makes it easier for the passive disk trapped between the rod and the wall to escape, and as soon as N changes from 1 to 0, the pressure quickly drives the surviving rod to absorption. This explains why both T_0 and T_1 decrease in the upper part of the intermediate range of ϕ where the hinge and a passive disk forms a stable motile clusteer (see Fig. 7d), completing a peak of the MFPT.

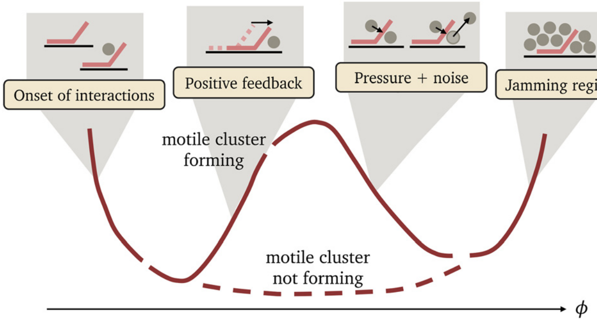

Fig. 8 Schematic of the four mechanisms contributing to the persistence of the motile state as ϕ is varied. The solid line represents the behaviors of the mean first-passage time (MFPT) of the active hinge for the case where a motile hinge–disk cluster forms. When ϕ is very small, presence of more passive particles quickens rotational diffusion by collisions, lowering the MFPT. As ϕ increases even more, it is more likely for a single passive disk to be trapped between the surviving rod and the wall, inducing persistent motion *via* positive feedback between cluster asymmetry and motility. If ϕ is increased further, pressure applied by the disks above the hinge slows its motion and makes it more likely for the escape of the trapped disk to lead to an immediate absorption, reducing the MFPT. In the jamming regime ($\phi \gtrsim 0.7$), the whole dynamics slow down, causing the MFPT to rise again. As indicated by the dashed line, the peak of the MFPT in the intermediate regime is not observed when Pe, l, $\theta_{\max}$, and μ are not large enough, hindering the formation of the motile hinge–disk cluster.

Based on these observations, we can identify four competing mechanisms that contribute to the lifetime of the motile state: (i) rotational diffusion of the surviving rod, whose activation *via* collisions with the passive disks causes a decrease in MFPT with ϕ when ϕ is small; (ii) positive feedback between cluster motility and asymmetry, which causes an increase in MFPT with ϕ (due to the higher probability of the passive disk becoming trapped between the hinge and the wall) when ϕ is in the lower intermediate range; (iii) pressure by the disks above the hinge combined with the noisy escape of the trapped passive disk, which causes a decrease in MFPT with ϕ (due to the hinge–wall gap quickly closing under the increased pressure as soon as the trapped passive disk leaves) when ϕ is in the upper intermediate range; (iv) jamming that slows down the dynamics and increases the MFPT when ϕ is very high. We again stress that the second and third of these mechanisms become significant only when all of Pe, l, $\theta_{\max}$, and μ are large enough, allowing strong cluster asymmetry and motility to develop. A schematic illustration of these mechanisms is provided in Fig. 8.

4.2 Effects of the maximum angle

We also discuss in detail how $\theta_{\max}$ affects the lifetime of the motile state. As noted in Section 4.1, higher $\theta_{\max}$ makes it easier for the system to form a symmetry-breaking motile structure, so the MFPT would naturally increase with $\theta_{\max}$. Here, we focus on the case $\phi = 0.7$, which roughly corresponds to the packing fraction used in the experiment of Son *et al.*,[45] although the results remain qualitatively similar even for ϕ as low as 0.3.

In Fig. 9, we show the MFPT as a function of $\theta_{\max}$ for different values of the dimensionless active force magnitude Pe (see Fig. 9a) and the rod length l (see Fig. 9b). While the MFPT generically increases with $\theta_{\max}$, it exhibits a particularly rapid growth when both Pe and l are large enough in the regime $\theta_{\max} \gtrsim 53^\circ$. These hint at a stabilization mechanism that is amplified only when the trap is strong enough and there is sufficient area beneath the surviving rod.

To gain more intuition into the origins of these behaviors, we examine the average time spent in each coarse-grained state

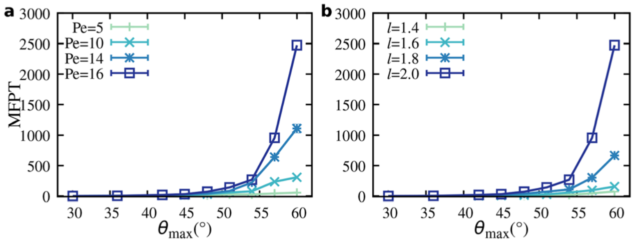

Fig. 9 Mean first-passage time (MFPT) as a function of the maximum angle at ϕ = 0.7 and μ = 40 for different active force magnitudes and rod length. (a) Active force dependence for l = 2. For Pe = 16, the lifetime of the motile state increases rapidly when $\theta_{\max}$ is increased beyond $\theta_{\max} \approx 53°$, so that three passive disks can form a stable triangular configuration between the rod and the wall. (b) Rod length dependence for Pe = 16. The abrupt increase on MFPT is not observed for smaller rod lengths. The error bars indicate the standard deviations, and the lines are to guide the eye.

N until absorption for different values of Pe in Fig. 10. As shown by both plots, if $\theta_{\max} \lesssim 53°$, the N = 1 state dominates the MFPT. This is because the circular sector between the rod and the wall is too narrow to allow any stable cluster of multiple passive disks. If $\theta_{\max} \gtrsim 53°$ and Pe = 5, then as shown in Fig. 10a, the N = 1 state still plays the role of a bottleneck while contributions from the other states remain small. However, if Pe = 16, Fig. 10b shows that the system spends a prolonged period of time in the N = 2 and N = 3 states. This is because three passive disks can form an extremely stable triangular cluster, as illustrated in Fig. 2c. Even if a single disk happens to leave the cluster, another disk will join the cluster with high probability. Moreover, the triangular cluster can also contribute to the N = 2 state since, even without the cluster disintegration, one of its disks can still fall outside the circular sector used to determine the value of N.

If Pe is not large enough, the forces trapping the cluster cannot hold it together for long, as reflected in the little time spent in the N = 3 state in Fig. 10a for Pe = 5. Although not included in this paper, we can also observe similar effects when either l or μ is not large enough.

As discussed in Section 2 (and illustrated in Fig. 1), $\theta_{\max}$ emulates the effects of the number of SPPs forming the cluster in the experiment of Son *et al.*[45] Our results corroborate the study's observation that the lifetime of the motile state exhibits an abrupt change as the number of SPPs is varied.

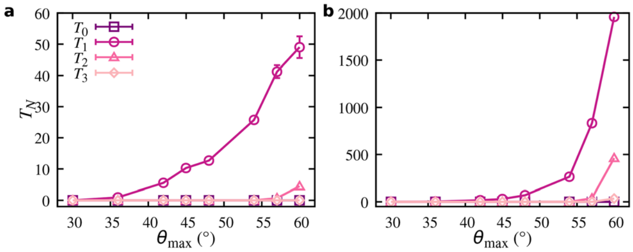

Fig. 10 Average time spent in each coarse-grained state N until absorption as a function of the maximum angle when ϕ = 0.7, l = 2, μ = 40 and (a) Pe = 5 or (b) Pe = 16. The error bars indicate the standard deviations, and the lines are to guide the eye.

5 Conclusions

Using extensive simulations of the active hinge model, which simplifies the dynamics of the self-propelled particle cluster at the boundary of a vibrated granular medium, we investigated how the packing fraction of the medium, the active force of the rods, the maximum angle between each rod and the boundary, the rods' length, and the hinge motility affect the motion of the cluster. Our results show that, even if the initial configuration of the hinge is fully symmetric, it takes much longer for the second rod to be absorbed compared to the first one due to the positive feedback between the asymmetry of the hinge and its motility. When the active force, maximum angle, rod length, and hinge mobility are all big enough, persistence of this mechanism exhibits a double-dipped dependence on the packing fraction, demonstrating the interplay of the positive feedback mechanism and the pressure exerted by the granular particles. Finally, as the maximum angle grows, we observe that the lifetime of the motile state increases by orders of magnitude since the configuration of the passive granular medium sustaining the motile state changes abruptly. This is analogous to how the active boundary cluster in the granular medium confined within a circular arena suddenly loses its motility as the number of active particles increases.[45]

These results demonstrate how an artificial system composed of a mixture of active and passive particles can self-organize to exhibit various dynamical modes by changing the number and physical properties of particles. In particular, if the boundary of the system is reshaped into a movable circular arena instead of the straight channel considered here, the motile and the immotile states of the active hinge will lead to straight and chiral motion of the whole superstructure, respectively. As suggested by our results, the switching between the two modes can be done by changing the area of the arena (which in turn changes the packing fraction) or the active force. Designing a mobile and steerable superstructure based on this principle may provide an interesting alternative to those utilizing interactions between active particles and soft membranes.[47,49,50]

Author contributions

L. G. Rigon: conceptualization, software, validation, formal analysis, investigation, writing – original draft, visualization. Y. Baek: conceptualization, methodology, supervision, writing – review & editing.

Conflicts of interest

There are no conflicts to declare.

Data availability

The computer codes used to generate the results of this paper are available at https://github.com/lgrigon/ActiveHingeModel.

Appendices

Appendix A. Overdamped equations of motion

Here, we derive the rigid-body dynamics of the active hinge in the overdamped limit and describe how we simulate it. Toward this end, we first need to connect the microscopic bead representation of each rod to the dynamics of the whole body constrained to the channel wall. More specifically, our goal is to obtain an effective drag matrix that relates the generalized velocities ($\dot{x}_{\mathrm{act}}$,$\dot{\theta}_{\mathrm{L}}$,$\dot{\theta}_{\mathrm{R}}$) to the net forces and torques acting on the system.

We have already assumed that each rod of the hinge consists of M beads, plus the central bead shared by both rods located at position x_{act}. Moreover, as illustrated in Fig. 2b, the left rod makes an angle θ_{L} with the x-axis, with bead positions given by $\mathbf{r}_i = (x_{\mathrm{act}} - r_i\cos\theta_{\mathrm{L}}, r_i\sin\theta_{\mathrm{L}})$ for $i = -M,\ldots,-1$, while the right rod makes an angle θ_{R} with the x-axis, with bead potions given by $\mathbf{r}_i = (x_{\mathrm{act}} + r_i\cos\theta_{\mathrm{R}}, r_i\sin\theta_{\mathrm{R}})$ for $i = 1,\ldots,M$. Putting $\mathbf{r}_0 = (x_{\mathrm{act}},0)$, we may indicate the central bead by the index $i = 0$.

Using these notations, the equation of motion for the generalized coordinates $q \in \{x_{\mathrm{act}},\theta_{\mathrm{L}},\theta_{\mathrm{R}}\}$ follows from Lagrange's equation

$$\frac{\mathrm{d}}{\mathrm{d}t}\frac{\partial L}{\partial \dot{q}} - \frac{\partial L}{\partial q} = -\frac{\partial G}{\partial \dot{q}} + \sum_{i=-M}^{M} \mathbf{F}_i \cdot \frac{\partial \mathbf{r}_i}{\partial q} + \frac{\partial}{\partial q}[\lambda_{\mathrm{L}} f_{\mathrm{L}}(\theta_{\mathrm{L}}) + \lambda_{\mathrm{R}} f_{\mathrm{R}}(\theta_{\mathrm{R}})], \tag{4}$$

where L is the Lagrangian (which, in this case, consists only of the kinetic energy) of the active hinge, G is the Rayleigh dissipation function, $\mathbf{F}_i$ is the net external force acting on the i-th bead, and $f_{\mathrm{L/R}}$ is the holonomic constraint applied on $\theta_{\mathrm{L/R}}$ whenever the angle is about to move beyond the range $[0,\theta_{\max}]$. For the updates during which $\theta_{\mathrm{L/R}}$ stays within this prescribed range, the corresponding Lagrangian multiplier $\lambda_{\mathrm{L/R}}$ can be put equal to zero.

Taking the overdamped limit, all masses of the active hinge vanish, erasing the effects of the Lagrangian. Then, we are left with

$$\frac{\partial G}{\partial \dot{q}} - \frac{\partial}{\partial q}[\lambda_{\mathrm{L}} f_{\mathrm{L}}(\theta_{\mathrm{L}}) + \lambda_{\mathrm{R}} f_{\mathrm{R}}(\theta_{\mathrm{R}})] = \sum_{i=-M}^{M} \mathbf{F}_i \cdot \frac{\partial \mathbf{r}_i}{\partial q}. \tag{5}$$

Denoting by $\gamma = 1/\mu$ the friction coefficient of each bead, the Rayleigh dissipation function reads

$$\begin{aligned} G &= \frac{\gamma}{2}\sum_{i=-M}^{M} \dot{\mathbf{r}}_i^{2} = \frac{\gamma}{2}\sum_{i=-M}^{-1}\left[\dot{x}_{\mathrm{act}}^{2} + 2r_i\dot{x}_{\mathrm{act}}\dot{\theta}_{\mathrm{L}}\sin\theta_{\mathrm{L}} + r_i^{2}\dot{\theta}_{\mathrm{L}}^{2}\right] \\ &\quad + \frac{\gamma}{2}\sum_{i=1}^{M}\left[\dot{x}_{\mathrm{act}}^{2} - 2r_i\dot{x}_{\mathrm{act}}\dot{\theta}_{\mathrm{R}}\sin\theta_{\mathrm{R}} + r_i^{2}\dot{\theta}_{\mathrm{R}}^{2}\right] + \frac{\gamma}{2}\dot{x}_{\mathrm{act}}^{2}. \end{aligned}$$

Assuming $r_i = r_{-i}$ and regrouping the terms, we obtain

$$\begin{aligned} G &= \frac{\gamma}{2}\Bigg\{(2M+1)\dot{x}_{\mathrm{act}}^{2} + 2\dot{x}_{\mathrm{act}}\left[\dot{\theta}_{\mathrm{L}}\sin\theta_{\mathrm{L}} - \dot{\theta}_{\mathrm{R}}\sin\theta_{\mathrm{R}}\right]\sum_{i=1}^{M} r_i \\ &\quad + \left(\dot{\theta}_{\mathrm{L}}^{2} + \dot{\theta}_{\mathrm{R}}^{2}\right)\sum_{i=1}^{M} r_i^{2}\Bigg\}. \end{aligned} \tag{6}$$

Using this in eqn (4), we obtain the overdamped equations of motion

$$\begin{aligned} &\gamma(2M+1)\dot{x} + \gamma\left[\dot{\theta}_{\mathrm{L}}\sin\theta_{\mathrm{L}} - \dot{\theta}_{\mathrm{R}}\sin\theta_{\mathrm{R}}\right]\sum_{i}^{M} r_i = \sum_{i=-M}^{M} F_{i,x} \equiv F_{\mathrm{tot},x}, \\ &\gamma\dot{\theta}_{\mathrm{L}}\sum_{i=-M}^{-1} r_i^{2} + \gamma\dot{x}\sin\theta_{\mathrm{L}}\sum_{i=-M}^{-1} r_i - \lambda_{\mathrm{L}} f'(\theta_{\mathrm{L}}) = -\sum_{i=-M}^{-1} \mathbf{r}_i \times \mathbf{F}_i \equiv \tau_{\mathrm{L}}\hat{\mathbf{z}}, \\ &\gamma\dot{\theta}_{\mathrm{R}}\sum_{i=1}^{M} r_i^{2} - \gamma\dot{x}\sin\theta_{\mathrm{R}}\sum_{i=1}^{M} r_i - \lambda_{\mathrm{R}} f'(\theta_{\mathrm{R}}) = \sum_{i=1}^{M} \mathbf{r}_i \times \mathbf{F}_i \equiv \tau_{\mathrm{R}}\hat{\mathbf{z}}, \end{aligned} \tag{7}$$

where $F_{\mathrm{tot},x}$ is the x-component of the net external force on the hinge, and τ_{L} and τ_{R} are the applied torques acting on the left and right rods (excluding the constraint torques), respectively. We note that the sign of τ_{L} (τ_{R}) has been chosen so that clockwise (counterclockwise) angular acceleration corresponds to $\tau_{\mathrm{L}} > 0$ ($\tau_{\mathrm{R}} > 0$).

Assuming equally spaced beads ($r_i = |i|l/M$), we can evaluate the sums of powers in the above equations as follows:

$$\begin{aligned} \sum_{i=1}^{M} r_i &= \frac{l}{2}(M+1), \\ \sum_{i=1}^{M} r_i^{2} &= \frac{l^{2}}{6M}(M+1)(2M+1). \end{aligned}$$

Substituting these into eqn (7), we obtain

$$\boldsymbol{\Gamma}\begin{pmatrix} \dot{x} \\ \dot{\theta}_{\mathrm{L}} \\ \dot{\theta}_{\mathrm{R}} \end{pmatrix} = \begin{pmatrix} F_{\mathrm{tot},x} \\ \tau_{\mathrm{L}} + \lambda_{\mathrm{L}} f'(\theta_{\mathrm{L}}) \\ \tau_{\mathrm{R}} + \lambda_{\mathrm{R}} f'(\theta_{\mathrm{R}}) \end{pmatrix}, \tag{8}$$

where the drag matrix is

$$\boldsymbol{\Gamma} = \gamma\begin{pmatrix} 2M+1 & \dfrac{l(M+1)}{2}\sin\theta_{\mathrm{L}} & -\dfrac{l(M+1)}{2}\sin\theta_{\mathrm{R}} \\ \dfrac{l(M+1)}{2}\sin\theta_{\mathrm{L}} & \dfrac{l^{2}}{6}\dfrac{(M+1)(2M+1)}{M} & 0 \\ -\dfrac{l(M+1)}{2}\sin\theta_{\mathrm{R}} & 0 & \dfrac{l^{2}}{6}\dfrac{(M+1)(2M+1)}{M} \end{pmatrix}. \tag{9}$$

As noted previously, this drag matrix couples translational and rotational degrees of freedom through the off-diagonal terms proportional to $\sin\theta_{\mathrm{L}}$ and $\sin\theta_{\mathrm{R}}$. In the absence of the constraint torques ($\lambda_{\mathrm{L}} = \lambda_{\mathrm{R}} = 0$), we finally reproduce eqn (1).

Enforcement of angular constraints. In the following, we describe how we simulate this overdamped equation of motion while ensuring that the rod angles stay within the range $[0,\theta_{\max}]$. For an update that would bring a rod beyond this range, we update the system during the period as if the rod was clamped at the boundary (that would have been crossed) throughout the time step. This clamping is enforced by setting

$$f_{\mathrm{L/R}}(\theta_{\mathrm{L/R}}) = \begin{cases} \theta_{\mathrm{L/R}} & \text{if } \theta_{\mathrm{L/R}} = 0 \text{ and } \tau_{\mathrm{L/R}} < 0, \\ \theta_{\mathrm{L/R}} - \theta_{\max} & \text{if } \theta_{\mathrm{L/R}} = \theta_{\max} \text{ and } \tau_{\mathrm{L/R}} > 0, \end{cases} \tag{10}$$

and finding the value of $\lambda_{\mathrm{L/R}}$ that ensures $\dot{\theta}_{\mathrm{L/R}} = 0$ in eqn (8).

Appendix B. MFPT estimation

The most straightforward way to estimate the MFPT is to obtain the sample mean of the first-passage time *via* numerous runs of the simulation. However, when the motile state exhibits a prolonged lifetime, there may be too few samples that reach the absorbing state, making the sample mean unreliable. To address this issue, we infer the MFPT from the survival probability of the rod, which is defined as

$$\mathrm{SP}(t) = \frac{1}{N_{\mathrm{sim}}} \sum_{i=0}^{N_{\mathrm{sim}}} H(\tau_i - t). \tag{11}$$

Here, N_{sim} is the number of simulation runs, τ_i is the absorbing time of the ith sample, and $H(x)$ is the Heaviside step function, which satisfies $H(\tau_i - t) = 1$ only before absorption of the rod ($t < \tau_i$) and $H(\tau_i - t) = 0$ otherwise. Assuming that the transient effects of the initial state quickly die out, we can expect the rod absorption to be a Poisson point process, so that the survival probability exhibits an exponential decay

$$\mathrm{SP}(t) \propto \mathrm{e}^{-\gamma t}. \tag{12}$$

After fitting the simulation data to infer the value γ, we use γ^{-1} as the estimator of the MFPT $\langle \tau \rangle$.

The average time T_N spent in a coarse-grained state N, where N is the number of passive disks below the rod, can be estimated by a similar method. For each value of N, we define

$$S(N,t) = \sum_{i=0}^{N_{\mathrm{sim}}} H\left(\sum_k \delta_{n_i(k\Delta t),N} \Delta t - t \right), \tag{13}$$

where Δt is the length of each discretized time step, and $n_i(k\Delta t)$ is the coarse-grained state of the ith sample at the kth time step. Then we infer T_N by fitting the data to $S(N,t) \sim \mathrm{e}^{-t/T_N}$.

Acknowledgements

L. G. R. and Y. B. were supported by the National Research Foundation of Korea (NRF) grants (RS-2023-00218318, RS-2023-00278985) funded by the Ministry of Science and ICT (MSIT) of the Korea government. Y. B. also acknowledge the support by Creative-Pioneering Researchers Program through Seoul National University.

References

1 S. Ramaswamy, *Annu. Rev. Condens. Matter Phys.*, 2010, **1**, 323–345.

2 M. C. Marchetti, J. F. Joanny, S. Ramaswamy, T. B. Liverpool, J. Prost, M. Rao and R. A. Simha, *Rev. Mod. Phys.*, 2013, **85**, 1143–1189.

3 C. Bechinger, R. Di Leonardo, H. Löwen, C. Reichhardt, G. Volpe and G. Volpe, *Rev. Mod. Phys.*, 2016, **88**, 045006.

4 S. Ramaswamy, *J. Stat. Mech.:Theory Exp.*, 2017, **2017**, 054002.

5 F. Jülicher, S. W. Grill and G. Salbreux, *Rep. Prog. Phys.*, 2018, **81**, 076601.

6 G. Gompper, R. G. Winkler and T. Speck, *et al.*, *J. Phys.:Condens. Matter*, 2020, **32**, 193001.

7 M. J. Bowick, N. Fakhri, M. C. Marchetti and S. Ramaswamy, *Phys. Rev. X*, 2022, **12**, 010501.

8 M. te Vrugt and R. Wittkowski, *Eur. Phys. J. E:Soft Matter Biol. Phys.*, 2025, **48**, 12.

9 L. Angelani and R. D. Leonardo, *New J. Phys.*, 2010, **12**, 113017.

10 A. Kaiser, A. Peshkov, A. Sokolov, B. ten Hagen, H. Löwen and I. S. Aranson, *Phys. Rev. Lett.*, 2014, **112**, 158101.

11 S. A. Mallory, C. Valeriani and A. Cacciuto, *Phys. Rev. E:Stat., Nonlinear, Soft Matter Phys.*, 2014, **90**, 032309.

12 F. Smallenburg and H. Löwen, *Phys. Rev. E:Stat., Nonlinear, Soft Matter Phys.*, 2015, **92**, 032304.

13 N. Koumakis, A. Lepore, C. Maggi and R. Di Leonardo, *Nat. Commun.*, 2013, **4**, 2588.

14 L. Angelani, R. Di Leonardo and G. Ruocco, *Phys. Rev. Lett.*, 2009, **102**, 048104.

15 A. Sokolov, M. M. Apodaca, B. A. Grzybowski and I. S. Aranson, *Proc. Natl. Acad. Sci. U. S. A.*, 2010, **107**, 969–974.

16 R. Di Leonardo, L. Angelani, D. Dell'Arciprete, G. Ruocco, V. Iebba, S. Schippa, M. P. Conte, F. Mecarini, F. D. Angelis and E. D. Fabrizio, *Proc. Natl. Acad. Sci. U. S. A.*, 2010, **107**, 9541–9545.

17 E. Tjhung, D. Marenduzzo and M. E. Cates, *Proc. Natl. Acad. Sci. U. S. A.*, 2012, **109**, 12381–12386.

18 G. De Magistris, A. Tiribocchi, C. A. Whitfield, R. J. Hawkins, M. E. Cates and D. Marenduzzo, *Soft Matter*, 2014, **10**, 7826–7837.

19 O. Granek, Y. Kafri and J. Tailleur, *Phys. Rev. Lett.*, 2022, **129**, 038001.

20 K.-W. Kim, Y. Choe and Y. Baek, *Phys. Rev. E*, 2024, **109**, 014614.

21 C. Wang, W. Lian, H. Li, W. Tian and K. Chen, *Natl. Sci. Open*, 2024, **3**, 20230066.

22 J.-H. Pei and C. Maes, *Phys. Rev. E*, 2025, **111**, L032101.

23 N. Nikola, A. P. Solon, Y. Kafri, M. Kardar, J. Tailleur and R. Voituriez, *Phys. Rev. Lett.*, 2016, **117**, 098001.

24 J. Shin, A. G. Cherstvy, W. K. Kim and V. Zaburdaev, *Phys. Chem. Chem. Phys.*, 2017, **19**, 18338–18347.

25 H.-S. Li, C. Wang, W.-D. Tian, Y.-Q. Ma, C. Xu, N. Zheng and K. Chen, *Soft Matter*, 2017, **13**, 8031–8038.

26 M. Shafiei Aporvari, M. Utkur, E. U. Saritas, G. Volpe and J. Stenhammar, *Soft Matter*, 2020, **16**, 5609–5614.

27 P. Melby, F. V. Reyes, A. Prevost, R. Robertson, P. Kumar, D. A. Egolf and J. S. Urbach, *J. Phys.: Condens. Matter*, 2005, **17**, S2689.

28 D. Yamada, T. Hondou and M. Sano, *Phys. Rev. E:Stat., Nonlinear, Soft Matter Phys.*, 2003, **67**, 040301.

29 A. Kudrolli, G. Lumay, D. Volfson and L. S. Tsimring, *Phys. Rev. Lett.*, 2008, **100**, 058001.

30 J. Deseigne, O. Dauchot and H. Chaté, *Phys. Rev. Lett.*, 2010, **105**, 098001.

31 J. Deseigne, S. Léonard, O. Dauchot and H. Chaté, *Soft Matter*, 2012, **8**, 5629–5639.

32 C. A. Weber, T. Hanke, J. Deseigne, S. Léonard, O. Dauchot, E. Frey and H. Chaté, *Phys. Rev. Lett.*, 2013, **110**, 208001.

33 M. Casiulis, E. Arbel, C. van Waes, Y. Lahini, S. Martiniani, N. Oppenheimer and M. Y. B. Zion, *Proc. Natl. Acad. Sci. U. S. A.*, 2025, **122**, e2502211122.

34 M. X. Lim, A. Souslov, V. Vitelli and H. M. Jaeger, *Nat. Phys.*, 2019, **15**, 460–464.

35 L. Caprini, D. Breoni, A. Ldov, C. Scholz and H. Lŏwen, *Commun. Phys.*, 2024, **7**, 343.

36 A. P. Antonov, M. Musacchio, H. Löwen and L. Caprini, *Nat. Commun.*, 2025, **16**, 7235.

37 G. Briand, M. Schindler and O. Dauchot, *Phys. Rev. Lett.*, 2018, **120**, 208001.

38 C. Scholz, M. Engel and T. Pöschel, *Nat. Commun.*, 2018, **9**, 931.

39 P. Digregorio, D. Levis, L. F. Cugliandolo, G. Gonnella and I. Pagonabarraga, *Soft Matter*, 2022, **18**, 566–591.

40 R. Ni, M. A. C. Stuart and M. Dijkstra, *Nat. Commun.*, 2013, **4**, 2704.

41 F. Kümmel, P. Shabestari, C. Lozano, G. Volpe and C. Bechinger, *Soft Matter*, 2015, **11**, 6187–6191.

42 B. van der Meer, L. Filion and M. Dijkstra, *Soft Matter*, 2016, **12**, 3406–3411.

43 N. Kumar, H. Soni, S. Ramaswamy and A. Sood, *Nat. Commun.*, 2014, **5**, 4688.

44 H. Soni, N. Kumar, J. Nambisan, R. K. Gupta, A. Sood and S. Ramaswamy, *Soft Matter*, 2020, **16**, 7210–7221.

45 K. Son, Y. Choe, E. Kwon, L. G. Rigon, Y. Baek and H.-Y. Kim, *Soft Matter*, 2024, **20**, 2777–2788.

46 J. Elgeti and G. Gompper, *Europhys. Lett.*, 2009, **85**, 38002.

47 A. Deblais, T. Barois, T. Guerin, P.-H. Delville, R. Vaudaine, J. S. Lintuvuori, J.-F. Boudet, J.-C. Baret and H. Kellay, *Phys. Rev. Lett.*, 2018, **120**, 188002.

48 H. Wensink and H. Löwen, *Phys. Rev. E:Stat., Nonlinear, Soft Matter Phys.*, 2008, **78**, 031409.

49 J.-F. Boudet, J. Lintuvuori, C. Lacouture, T. Barois, A. Deblais, K. Xie, S. Cassagnere, B. Tregon, D. B. Brückner and J.-C. Baret, *et al.*, *Sci. Rob.*, 2021, **6**, eabd0272.

50 S. Y. Lee, P. W. Schönhöfer and S. C. Glotzer, *Sci. Rep.*, 2023, **13**, 22773.